Chemical Engineering Journal 435 (2022) 134860

Contents lists available at ScienceDirect

Chemical Engineering Journal

journal homepage: www.elsevier.com/locate/cej

High-performance alkaline water splitting by Ni nanoparticle-decorated Mo-Ni microrods: Enhanced ion adsorption by the local electric field

HuangJingWei Li [a], Chao Cai [a], Qiyou Wang [a], Shanyong Chen [a], Junwei Fu [a], Bao Liu [a], Qingnan Hu [a], Kangman Hu [a], Hongmei Li [a], Junhua Hu [b], Qiming Liu [c], Shaowei Chen [c,*], Min Liu [a,*]

[a] School of Physics and Electronics, Hunan Joint International Research Center for Carbon Dioxide Resource Utilization, Central South University, Changsha 410083, China
[b] School of Materials Science and Engineering, Zhengzhou University, Zhengzhou 450001, China
[c] Department of Chemistry and Biochemistry, University of California, 1156 High Street, Santa Cruz, CA 95064, United States

ARTICLE INFO

Keywords:
Local electric field
MEA
Mo-based
Ni nanoparticle
Alkaline water splitting

ABSTRACT

Hydrogen production by alkaline water electrolysis represents an effective route for low-cost and clean energy conversion. However, as hydrogen ions (H^+) are the minority species in alkaline media, the kinetics of hydrogen evolution reaction (HER) is markedly reduced. Concurrently, the transport of hydroxide ions (OH^-) is limited under large current density in alkaline oxygen evolution reaction (OER). Herein, Ni nanoparticles-decorated Mo-Ni microrods (Ni/Mo-Ni) are adopted to boost the ion adsorption. Finite-element simulations suggest that a strong local electric field around the Ni nanoparticles exponentially increases ion adsorption towards the electrode surface, which facilitates reaction kinetics and mass transfer for HER at the cathode and OER at the anode. Thus, the Ni/Mo-Ni electrode exhibits a low overpotential of only −24 mV for HER and + 215 mV for OER to reach the current density of 10 mA cm^{-2}, and can achieve an industrial alkaline splitting current density of 100 mA cm^{-2} at a low voltage of 1.76 V and stably operate for 87 h. This work suggests a new paradigm in the design and engineering of high-performance catalysts for alkaline electrolyzers.

1. Introduction

Alkaline water splitting is a promising approach to the production of clean hydrogen energy, which is widely considered as an important chemical resource and promising energy carrier [1–6]. Water-alkali electrolyzers have been hailed as an attractive technology for the industrial production of hydrogen [7–10]. However, the low hydrogen ion (H^+) concentration in alkaline media has been known to hamper the kinetics of the hydrogen evolution reaction (HER), resulting in an activity 2 to 3 orders of magnitude lower than that in acidic media and hence a low efficiency of water splitting [10–13]. Meanwhile, the transport of hydroxide ion (OH^-) is a limitation under large current density in oxygen evolution reaction (OER) at the anode [14–18]. One can envision that surface enrichment of H^+ and OH^- can significantly boost the efficacy of both HER and OER, if such an ion-enhanced environment can be enabled at the electrode surfaces.

Recently, the electric field-induced reagent concentration (FIRC) effect has attracted great attention in electrocatalysis. In previous studies [19–22], we observed that a high local electric field (LEF) could improve the catalytic activity. For instance, the LEF generated on the tips of Au nanoneedles induced K^+ aggregation and high CO_2 concentration around the active sites and greatly promoted CO_2 reduction reaction (CO_2RR) on the Au nanoneedles [19]. Yang's group demonstrated that the LEF at the tips of PtNi and NiFe facilitated the selective adsorption of H^+ and OH^-, leading to enhanced performance towards alkaline HER and OER, respectively [14,23]. Yet, despite the progress, the cell voltages in full water splitting have remained large with such catalysts, and there is an urgent need to develop high-efficiency and low-cost electrocatalysts for full water splitting where large current densities at low voltage can be produced.

Transition metal oxides have sparked considerable interest as viable electrocatalysts owing to their excellent activity and durability [24–26], and the activity can be further enhanced by deliberate structural engineering, such as vacancy engineering [27], formation of nanointerfaces

* Corresponding authors.
E-mail addresses: shaowei@ucsc.edu (S. Chen), minliu@csu.edu.cn (M. Liu).

https://doi.org/10.1016/j.cej.2022.134860
Received 23 November 2021; Received in revised form 15 January 2022; Accepted 19 January 2022
Available online 25 January 2022

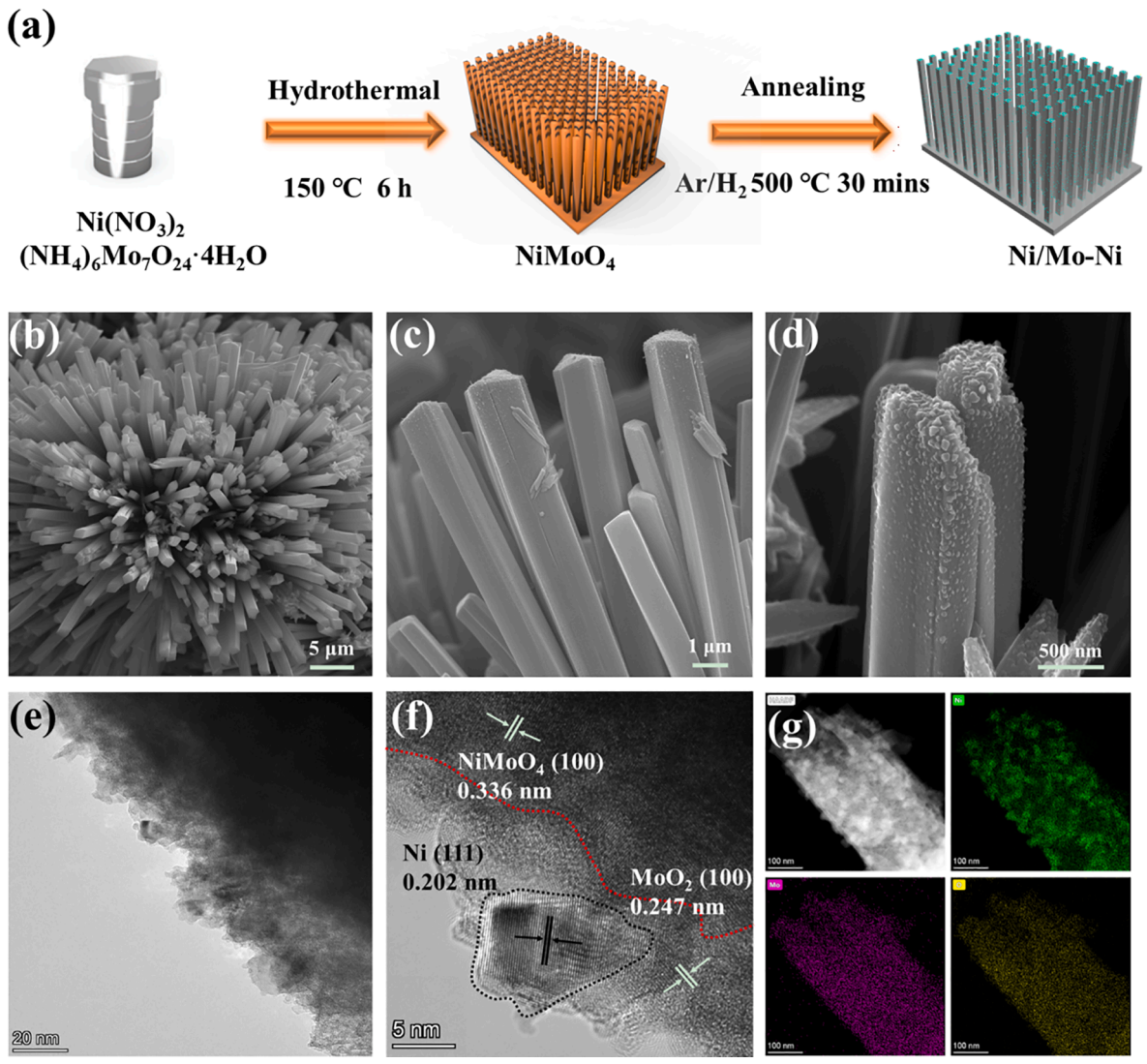

Fig. 1. (a) Schematic illustration of the synthesis of Ni/Mo-Ni. (b-d) SEM images of Ni/Mo-Ni at different magnifications. (e-f) HRTEM images of Ni/Mo-Ni at different magnifications, and (g) the corresponding elemental maps of Ni, Mo, and O.

[28,29], and electronic modulation [30,31]. For example, oxygen vacancies in $MoO_2/NiMoO_4$ hybrids have been found to serve as active sites responsible for the high performance in water splitting [27]. Nevertheless, studies have been scarce focusing on the effect of ion adsorption on the efficacy of water splitting.

In the present study, we prepared Ni nanoparticles-decorated Mo-Ni microrods (Ni/Mo-Ni) nanostructures via a facile hydrothermal method, which needed a low overpotential (η_{10}) of only −24 mV in HER and + 215 mV in OER to reach the current density of 10 mA cm^{-2} in alkaline media. Finite-element simulations demonstrated that a strong local electric field around the Ni nanoparticles exponentially increased the ion adsorption towards the electrode surface, which facilitated reaction kinetics and mass transfer for HER at the cathode and OER at the anode. The obtained Ni/Mo-Ni electrodes were used as bifunctional catalysts for industrial alkaline water splitting requiring only a cell voltage of 1.50, 1.76, and 1.87 V to reach the current density of 10, 100, and 400 mA cm^{-2}, respectively, and could stably operate for 87 h. This performance is markedly better than that with commercial Pt/C-IrO_2 catalysts.

2. Experimental section

2.1. Materials

Ammonium molybdate tetrahydrate ($(NH_4)_6Mo_7O_{24}·4H_2O$), nickel (II) nitrate ($Ni(NO_3)_2·6H_2O$), potassium hydroxide (KOH), carboxymethyl carboxyethyl cellulose (HECMC), nickel chloride ($NiCl_2·6H_2O$), hydratehydrazine, and platinum on graphitized carbon (20 wt% Pt/C) were purchased from Aladdin Reagents Co., Ltd. Deionized water (MillQ, 18.2 MΩ cm) was used throughout the entire study.

2.2. Sample preparation

Firstly, a piece of Ni Foam (NF) was sonicated in 3.0 M HCl for 10 min to remove the NiO layer on the surface, washed with ethanol and deionized water, and dried in air. $NiMoO_4$ precursors were synthesized by a hydrothermal method. In brief, 40 mmol of $Ni(NO_3)_2·6H_2O$ and 10 mmol of $(NH_4)_6Mo_7O_{24}·xH_2O$ were dissolved in 30 mL of deionized water. After gentle stirring for 30 min, the solution was transferred to a 50 mL Teflon-lined stainless steel autoclave with a piece of the clean NF (2 cm × 3 cm). The autoclave was sealed and heated at 150 °C for 6 h in an oven and then cooled down to room temperature naturally. Finally,

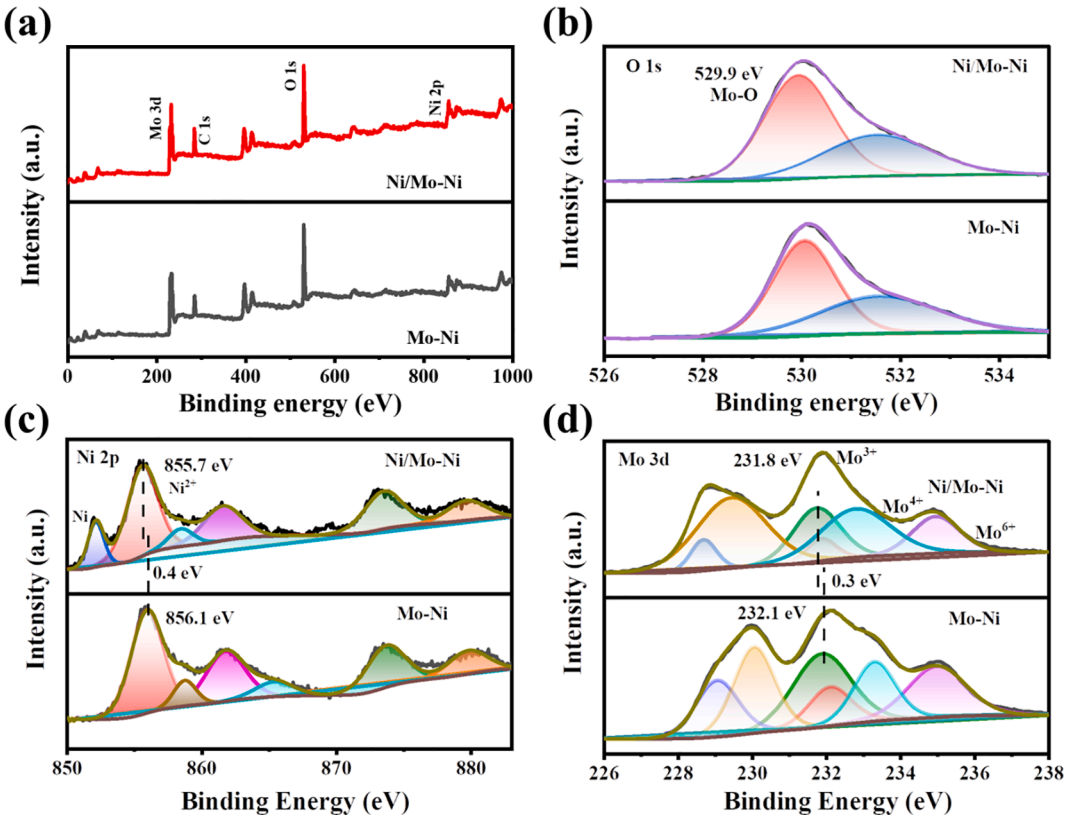

Fig. 2. (a) XPS survey spectrum of Ni/Mo-Ni and the corresponding high-resolution scans of the (b) O 1 s, (c) Ni 2p, and (d) Mo 3d electrons of Ni/Mo-Ni and Mo-Ni. In panels (b), (c), and (d), black curves are experimental data and colored peaks are deconvolution fits.

the product was taken out, rinsed with deionized water and ethanol several times, and dried at 60 °C in air. The obtained $NiMoO_4$ precursor was then heated in a tube furnace at 500 ℃ for 30 min under an H_2/Ar (10%) atmosphere, affording Ni nanoparticles-decorated MoO_2/$NiMoO_4$ microrod arrays. The final product was denoted as Ni/Mo-Ni. Two additional samples were prepared in the same manner except that the heating time was varied to 15 min and 2 h, and referred to as Ni/Mo-Ni@15 mins, and Ni/Mo-Ni@2h, respectively.

The surface Ni nanoparticles were removed by immersing Ni/Mo-Ni into 3 M HCl for 6 h, and the remaining solids (Mo-Ni) were collected by centrifugation, rinsed with deionized water and ethanol several times, and dried at 60 °C in air.

2.3. Characterizations

The crystalline structures of the samples prepared above were characterized *via* powder X-ray diffraction (XRD) with a Rigaku D/Max-2550 diffractometer. Scanning electron microscopy (SEM) studies were performed with an FEI Quanta 3D field-emission scanning electron microscope. Transmission electron microscopy (TEM) images were obtained on an FEI TF20 TEM microscope, where energy-dispersive X-ray (EDX) spectroscopy-based elemental mapping measurements were conducted. X-ray photoelectron spectroscopy (XPS) measurements were performed on a Thermo Fisher ESCALAB 250Xi spectrometer using monochromatized Al K_α excitation, where the binding energies were calibrated against the C 1 s peak at 284.8 eV.

2.4. Electrochemical measurements

Electrochemical measurements were performed in a three-electrode system. The data were collected by using a Princeton electrochemical workstation. The Ni/Mo-Ni sample prepared above, carbon rod, Ag/AgCl in saturated KCl were used as the working, counter, and reference electrodes, respectively (the corresponding catalyst loading was ca. 2.5 mg cm^{-2}). Comparative studies were also conducted with Pt/C at the mass loading of 2.5 mg cm^{-2}. Linear sweep voltammetry (LSV) of HER and OER was performed in a 1 M KOH solution at a scan rate of 2 mV s^{-1}. All polarization curves were recorded with manual iR-correction, and the potentials were converted to the reversible hydrogen electrode (RHE), $E_{RHE} = E_{Ag/AgCl} + 0.197 + 0.0591pH$. The solution was deaerated with N_2 gas for 20 min before HER/OER measurements. Cyclic voltammetry (CV) was conducted to test the long-term stability at a sweep rate of 100 mV s^{-1}. Electrochemical impedance spectra were acquired within the frequency range of 100 kHz to 0.1 Hz.

3. Results and discussion

3.1. Structural characterizations

As illustrated in Fig. 1**a,** Ni/Mo-Ni microrod arrays were synthesized via a two-step procedure: (a) hydrothermal synthesis of $NiMoO_4$ microrod arrays on NF using $Ni(NO_3)_2{\cdot}6H_2O$ and $(NH_4)_6Mo_7O_{24}{\cdot}xH_2O$ as the precursors, and (b) thermal treatment of $NiMoO_4$ under a hydrogen atmosphere [11,32–34]. From the SEM images in Fig. 1**b-d**, the produced Ni/Mo-Ni catalyst can be seen to exhibit a microrod morphology, which consisted of a rather dense array of microrods of ca. 1 μm in diameter and 16 μm in length. High-resolution TEM measurements (Fig. 1**e-f**) show that the microrod surfaces were decorated with a number of small nanoparticles of ca. 10 nm in diameter. Both the nanoparticles and microrods exhibited well-defined lattice fringes, with an interplanar spacing of 0.202 nm for the nanoparticles and 0.247 nm and 0.336 nm for the microrods that can be assigned to the Ni(1 1 1), MoO_2(1 0 0), and $NiMoO_4$(1 0 0) planes, respectively [35–38]. In EDX-based elemental mapping analysis (Fig. 2**g**), the Ni, Mo, and O elements can be found across the sample, and the distributions of Mo and O were rather even, whereas Ni was enriched within the nanoparticles.

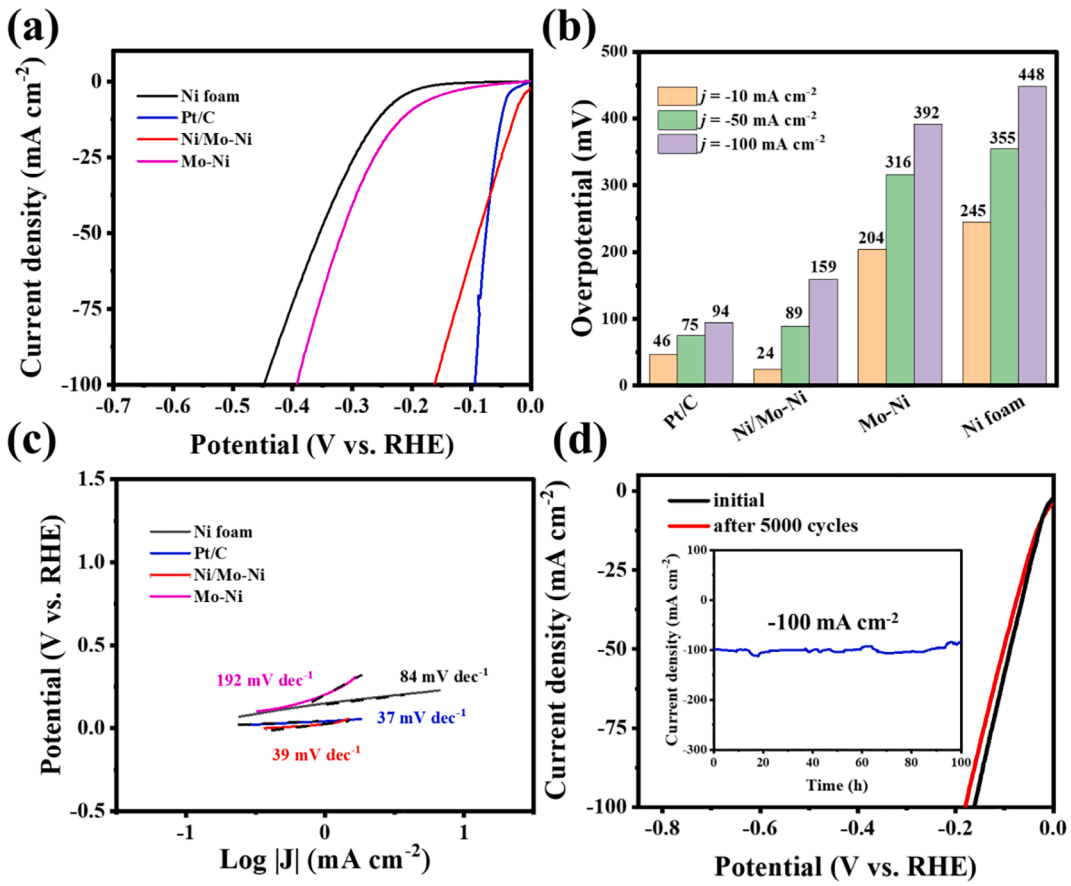

Fig. 3. (a) HER polarization curves of nickel foam, Mo-Ni, Ni/Mo-Ni, and Pt/C in 1 M KOH. (b) The corresponding overpotentials at the current density (j) of 10, 50, and 100 mA cm^{-2} and (c) Tafel slopes. (d) HER polarization curves of the Ni/Mo-Ni electrode before and after 5000 CV cycles, along with the chronoamperometric test for 100 h at −0.16 V vs. RHE (inset).

The surface Ni nanoparticles could be readily removed by HCl etching, as evidenced in SEM measurements (**Figure S1**), where the resulting Mo-Ni microrods exhibited a mostly smooth surface.

The crystal structures of the obtained samples were then examined by XRD measurements. To minimize background interference, the sample was scratched off from the NF. From **Figure S2**, the Ni/Mo-Ni sample can be seen to exhibit four sharp peaks at 2θ = 37.3°, 43.9°, 51.5°, and 63.3°, which can be ascribed to the (1 0 0) facets of MoO_2 (JCPDS 50–0739), (1 1 1) facets of Ni (JCPDS 04–0850), (1 0 0) facets of Ni (JCPDS 04–0850), and (1 0 0) facets of $NiMoO_4$ (JCPDS 13–0128) [28,39–41], respectively. The elemental composition and valence state was then probed by XPS measurements. From the survey spectrum in Fig. 2**a**, the elements of Ni (875 eV), Mo (232 eV), O (530 eV), and C (284 eV) can be readily identified in Ni/Mo-Ni. As shown in Fig. 2**b**, the high-resolution scans of the O 1 s electrons include a peak at 529.9 eV corresponding to Mo-O bonds [29]. The high-resolution scans of the Ni 2p electrons are shown in Fig. 2**c**. Deconvolution of the Ni/Mo-Ni spectrum yields a doublet at 852.8/870.1 eV for the $2p_{3/2}/2p_{1/2}$ electrons of metallic Ni [9], and another one at 855.7/873.1 eV for Ni^{2+} [22]. From the Mo 3d spectrum in Fig. 2**d**, three doublets can be deconvoluted for the $3d_{5/2}/3d_{3/2}$ electrons of Mo^{3+} at 228.7/231.8 eV, Mo^{4+} at 229.5/232.8 eV, and Mo^{6+} at 231.8/234.9 eV [42–45]. After removal of the Ni nanoparticles by acid etching (Fig. 2**c and 2d**), the metallic Ni peaks disappeared, and the Ni^{2+} 2p and Mo^{3+} 3d peaks shift to a higher energy by ~ 0.4 eV and ~ 0.3 eV, respectively, suggesting electron transfer from Ni nanoparticles to Mo-Ni in Ni/Mo-Ni.

3.2. Electrocatalytic activity

We then assessed the samples' electrocatalytic activities towards HER in 1 M KOH with a standard three-electrode system. From the HER polarization curves in Fig. 3**a**, one can see that in comparison to bare NF, the activity of Mo-Ni was apparently improved. Further enhancement can be observed with Ni/Mo-Ni, which even outperformed commercial Pt/C at low overpotentials. The $\eta_{10,HER}$ value can be seen to vary in the order of Ni foam (-245 mV) > Mo-Ni (-204 mV) > Pt/C (-46 mV) > Ni/Mo-Ni (-24 mV) (Fig. 3**b**). The corresponding Tafel slope was estimated to be 39 mV dec^{-1} for Ni/Mo-Ni, which is slightly greater than that of Pt/C (37 mV dec^{-1}), but significantly lower than those of Mo-Ni (192 mV dec^{-1}) and nickel foam (84 mV dec^{-1}) (Fig. 3**c**) - this is consistent with the increasing overpotential of Ni/Mo-Ni, as compared to Pt/C. The fact that the HER activity of Ni/Mo-Ni was drastically better than that of Mo-Ni suggests the significant role of Ni nanoparticles in boosting the HER electrocatalysis.

As shown in **Figure S3**, the Ni/Mo-Ni electrode exhibited the largest double-layer capacitance (C_{dl}, 0.696 mF cm^{-2}), as compared to bare NF (0.540 mF cm^{-2}) and Mo-Ni (0.169 mF cm^{-2}), suggesting the largest electrochemical surface area (ECSA) among the series in HER (Table S1). Consistent results were obtained in electrochemical impedance spectroscopic measurements at −0.025 V (**Figure S4** and Table S2), where Ni/Mo-Ni was found to possess the lowest charge transfer resistance (R_{ct}) of 2.25 Ω, as compared to 3.87 Ω for Mo-Ni and 7.81 Ω for pristine NF. To further evaluate the intrinsic electrocatalytic activity of these catalysts for HER, the turnover frequency (TOF) was also computed and compared, and Ni/Mo-Ni shows a TOF of 0.052 s^{-1} (**Figure S5**) markedly larger than those of Mo-Ni (0.0019 s^{-1}) and pristine NF (0.0017

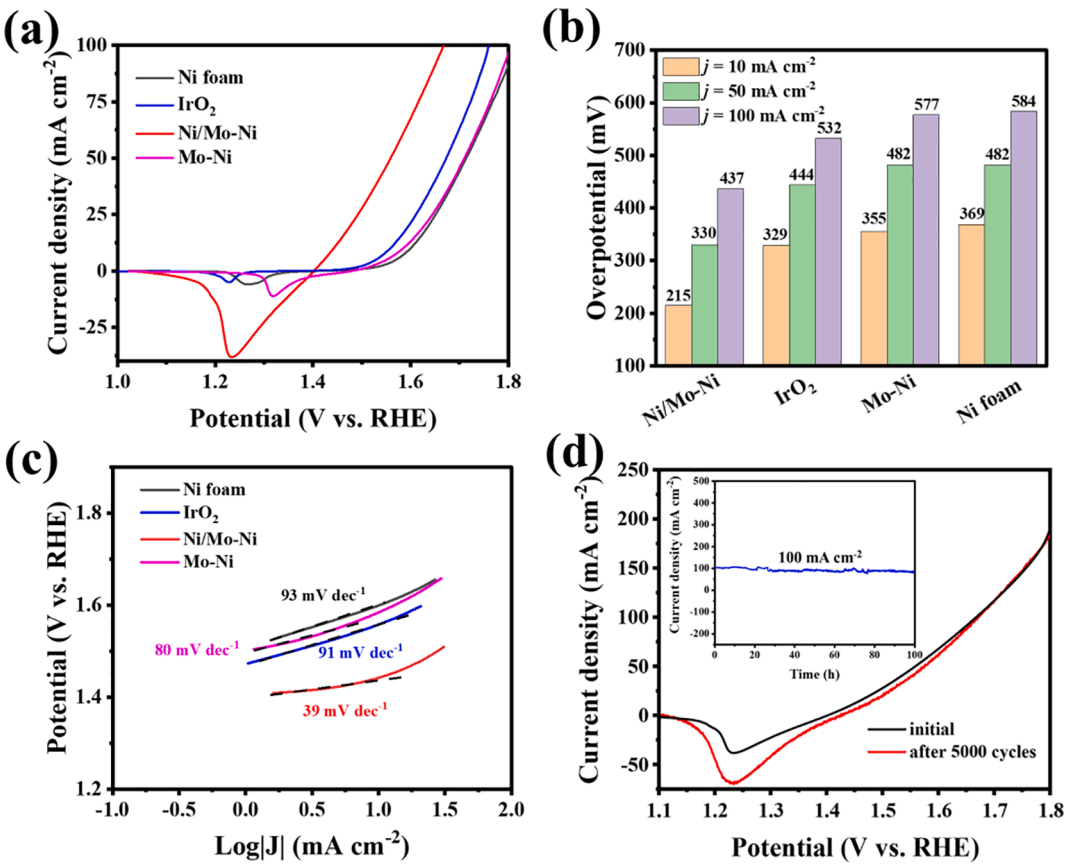

Fig. 4. (a) OER polarization curves of nickel foam, Mo-Ni, Ni/Mo-Ni, and Pt/C in 1 M KOH. (b) The corresponding overpotentials at the current density (j) of 10, 50, and 100 mA cm^{-2} and (c) Tafel plot. (d) OER polarization curves of the Ni/Mo-Ni electrode before and after 5000 CV cycles. along with the chronoamperometric test for 100 h at 1.67 V vs. RHE (inset).

s^{-1}).

The Ni/Mo-Ni electrode also shows good durability in alkaline solutions. The polarization curve remained virtually unchanged after 5000 potential cycles (Fig. 3**d**). In addition, we explore the long-term stability of the electrocatalyst tested at the fixed at −0.16 V vs. RHE, the Ni/Mo-Ni electrode current density of 100 mA cm^{-2} remained almost invariant for 100 h (Fig. 3**d inset**). Notably, the morphology and XRD patterns of the electrocatalyst stayed unchanged even after these long-term durability tests, attesting to the superb structural stability of the catalysts (**Figure S6 and S7**). In fact, the HER performance (e.g., Tafel slope and $\eta_{10,HER}$) of Ni/Mo-Ni was superior or highly comparable to leading results of Ni- and Mo-based catalysts reported recently in the literature (Table S3).

The OER activity of the prepared electrocatalysts was also studied in the same solution. From the OER polarization curves in Fig. 4**a**, one can see that the Ni/Mo-Ni electrode again exhibited the best performance among the series, with an ultra-low $\eta_{10,OER}$ of + 215 mV, in comparison to + 329 mV for IrO_2, +355 mV for Mo-Ni, and + 369 mV for Ni foam; and a similar trend can be seen at other current densities (Fig. 4**b**). The Ni/Mo-Ni electrode also displays a lower Tafel slope (39 mV dec^{-1}) than IrO_2 (91 mV dec^{-1}), Mo-Ni (80 mV dec^{-1}), and Ni foam electrodes (93 mV dec^{-1}) (Fig. 4**c**). As shown in **Figure S8**, the Ni/Mo-Ni electrode also exhibited the largest double-layer capacitance (C_{dl}, 1.92 mF cm^{-2}), as compared to Ni Foam (0.97 mF cm^{-2}) and Mo-Ni (1.73 mF cm^{-2}), suggesting the largest ECSA among the series in OER **(**Table S4**)**.

Consistent results were obtained in electrochemical impedance spectroscopic measurements at + 1.48 V (**Figure S9** and Table S5), where Ni/Mo-Ni was found to possess the lowest R_{ct} of 0.37 Ω, as compared to 4.84 Ω for pristine NF and 1.13 Ω for Mo-Ni. The TOF_{OER} values of these electrocatalysts are also shown in **Figure S5c**, where Ni/Mo-Ni reveals a value of 0.171 s^{-1}, much higher than Mo-Ni (0.003 s^{-1}) and Ni foam (0.0023 s^{-1}), confirming the superior intrinsic electrocatalytic activity of Ni/Mo-Ni for OER. The Ni/Mo-Ni electrode also shows good durability in OER. The polarization curve exhibited only a small change after 5000 potential cycles (Fig. 4**d**). Moreover, the Ni/Mo-Ni electrode shows high stability in a long time at the fixed at 1.67 V vs. RHE (Fig. 4**d inset**), the current density was largely invariant for over 100 h. Notably, the OER performance (e.g., Tafel slope and $\eta_{10,\ OER}$) of Ni/Mo-Ni was highly comparable or even superior to Ni- and Mo-based catalysts reported recently in the literature (Table S6).

Encouraged by the outstanding bifunctional activity of the Ni/Mo-Ni electrode, Ni/Mo-Ni was used as both the cathode and anode catalysts, separated with a FAB-3-pk-130 membrane, for an AEM-based water electrolyzer in a flowing 1 M KOH solution (Fig. 5**a** and **insets to** Fig. 5**d**). From Fig. 5**b**, one can see that the electrolyzer needed a cell voltage of only 1.50, 1.66, and 1.76 V to drive water splitting at the current density of 10, 50, and 100 mA cm^{-2}, respectively. The performance was markedly better than that based on commercial Pt/C (cathode) and IrO_2 (anode) catalysts or based on NF alone (Fig. 5**c**). In general, a 2.4 V cell voltage is needed to drive 400 mA cm^{-2} in commercial alkaline water electrolysis; yet with the prepared Ni/Mo-Ni electrodes, an ultralow cell voltage of 1.87 V was needed to generate such a current density, demonstrating the superior performance of the Ni/Mo-Ni electrolyzer in full water splitting, as compared to leading results reported recently in the literature with relevant bifunctional electrocatalysts (Table S7). Hydrogen was continuously generated at the rate of 6.35 mL min^{-1} at a fixed current density of 100 mA cm^2 for 2500 s, as shown in **Figure S10**; and the AEM system maintained a high energy efficiency of around 72 %. The Ni/Mo-Ni electrolyzer also exhibited high stability. At the cell voltage of 1.76 V, the current density remained

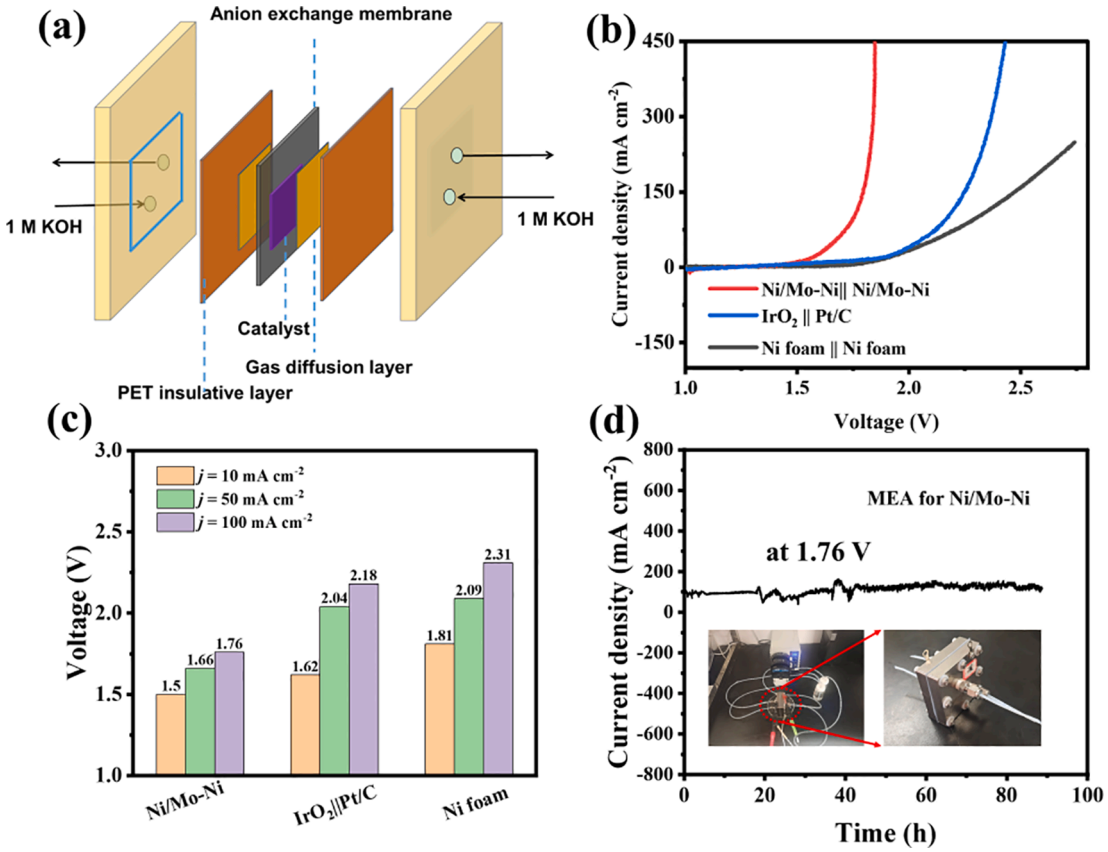

Fig. 5. (a) Schematic illustration of the AEM electrolyzer. (b) Water splitting polarization curves with varied electrode catalysts at the anode and cathode in 1 M KOH; and (c) the corresponding cell voltages at the current density of 10, 50, and 100 mA cm^{-2}. (d) Water splitting current density of the Ni/Mo-Ni AEM electrolyzer at the cell voltage of 1.76 V. Insets are the photographs of the AEM electrolyzer.

virtually invariant at 100 mA cm^{-2} for over 87 h's continuous operation (Fig. 5**d**).

To evaluate the Faraday efficiency, the Ni/Mo-Ni samples were used as both the cathode and anode, and the produced H_2 and O_2 gases were collected using a drainage method in a two-electrode configuration at 10 mA cm^{-1} for 1250 s. As shown in **Figure S11-S12**, the produced H_2 to O_2 showed a volume ratio of 2.13:1, very close to the theoretical value of 2:1, and the Faradaic efficiency was estimated to be ca. 99.5% (details in the Supporting Information). This result confirms that Ni/Mo-Ni can indeed be used as an efficient and durable electrocatalyst toward water splitting.

3.3. *Theoretical simulations and OH^- measurments*

To unravel the mechanistic origin of the remarkable electrocatalytic activity, finite element simulations based on COMSOL were carried out to probe the LEF on the microrod surface. 2D models were constructed to represent the electric field distribution on the surface of a smooth Mo-Ni structure with and without Ni nanoparticles. As shown in Fig. 6**a1-6a2**, for the smooth Mo-Ni structure, a high electric field appears only near the corner of the Mo-Ni microrods during HER electrocatalysis. Yet for Ni/Mo-Ni where the Mo-Ni surface was decorated with many Ni nanoparticles (with a surface coverage of ca. 80 per μm^2, **Figure S13**), a high electric field (red regions in the figure) can be found surrounding each of the Ni nanoparticles. These hot spots were distributed around the entire electrode surface and significantly altered the reaction kinetics at the corner areas, which is believed to be the major driving force in enhancing the catalytic activity [46,47]. In addition, these hot spots greatly increased the reactive surface area of the Mo-Ni microrods. That is, the formation of a local high-curvature morphology by Ni nanoparticles in Ni/Mo-Ni increased the catalytic activity by widening the distribution of a high local electric field across the Mo-Ni surface. A similar enhanced electric field is observed in OER electrocatalysis (Fig. 6**b1-6b2**).

Notably, around the Ni particles, the H^+ and OH^- concentrations were significantly enhanced during HER and OER, respectively. The models were constructed to evaluate the OH^- concentration distributions on the microrod structure in an electrolyte solution. In a quasi-static simulation condition, the electric field can reach 0.8 V μm^{-1} at the smooth Mo-Ni model (Fig. 6**c and** Table S8), with an OH^- concentration of 1 mol L^{-1} (Fig. 6**a3**) in HER. By contrast, the electric field is markedly stronger at 2 V μm^{-1} for the Ni/Mo-Ni structure, and the repulsion of OH^- is far higher than that on smooth Mo-Ni (Fig. 6**a4**). These results demonstrated higher H^+ accumulation on the Ni/Mo-Ni surface. In OER, the same ion-enhanced situation occurs and the concentrate of OH^- is higher than that on smooth Mo-Ni around the high-curvature Ni nanoparticles (Fig. 6**b3-6b4**). In HER, OH^- decreased as the electric field increased, whereas in OER, OH^- increased with the increase of the electric field (Fig. 6**c**). Based on the above results, one can see that the Ni nanoparticles on the Mo-Ni surface provide a local electrical field, where the resultant local ion-enhanced environment facilitated the catalytic reaction and hence improved the performance in alkaline water splitting (Fig. 6**d**).

Note that the above Ni/Mo-Ni sample was prepared by thermal treatment at 500 °C for 30 min, and the electrocatalytic performance was markedly better than the control samples prepared at either shorter or longer heating (i.e., Ni/Mo-Ni@15 mins and Ni/Mo-Ni@2h) or Ni nanoparticles alone. From the SEM images in **Figure S14-15**, one can see that the Ni/Mo-Ni sample contained a higher number of nanoparticles than Ni/Mo-Ni@15 mins; and as the annealing time was prolonged to 2 h (Ni/Mo-Ni@2h), the sample surface became fully covered with much larger nanoparticles and the substrate no longer becomes

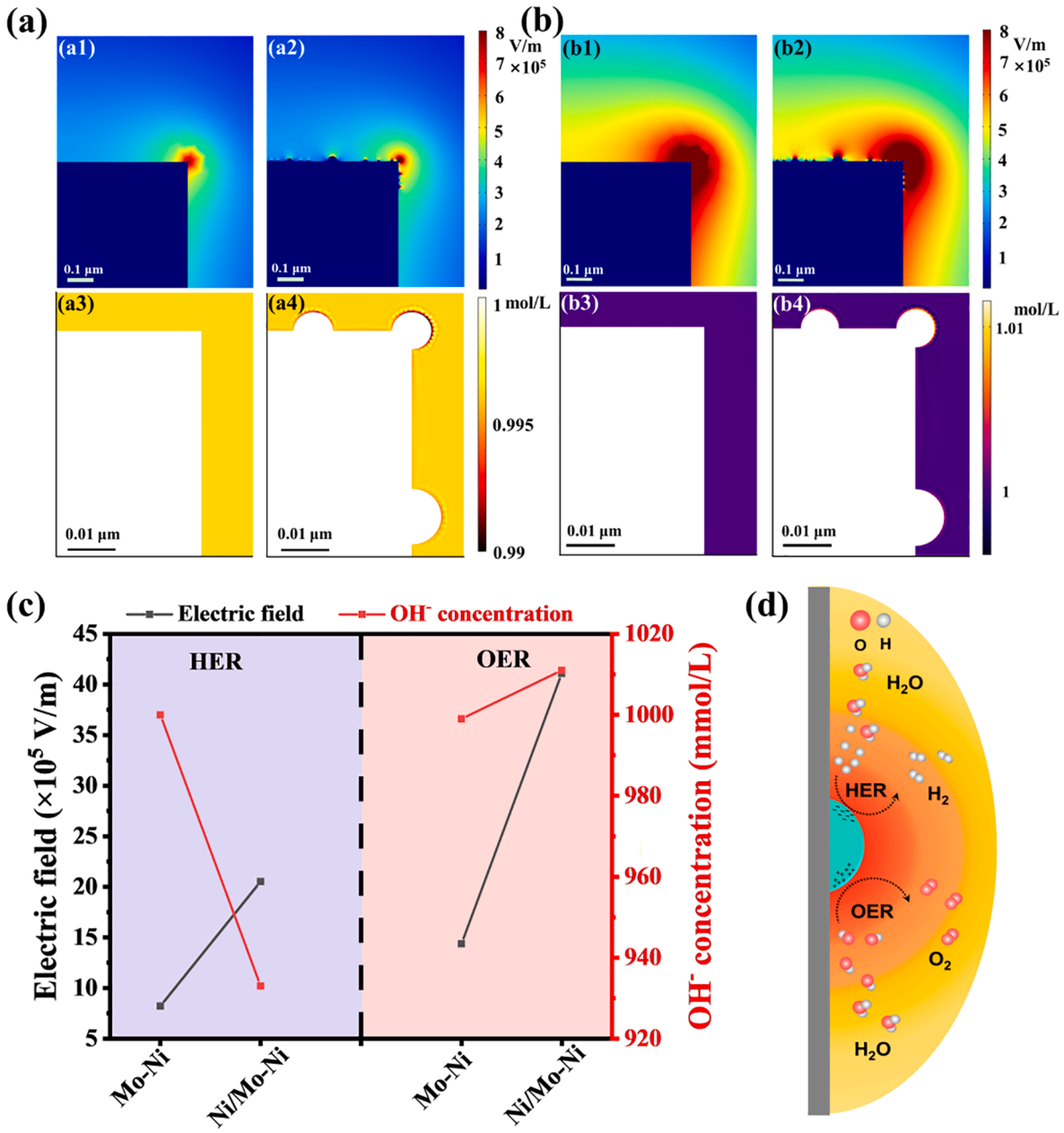

Fig. 6. COMSOL simulation of the electronic field and ion concentration in HER and OER. (a) Electric field at the microrod surface of (a1) smooth Mo-Ni and (a2) Ni/Mo-Ni, and the corresponding OH^- concentration distribution at the (a3) smooth Mo-Ni and (a4) Ni/Mo-Ni in HER. (b) Electric field of (b1) smooth Mo-Ni and (b2) Ni/Mo-Ni, and the corresponding OH^- concentration on the (b3) smooth Mo-Ni and (b4) Ni/Mo-Ni in OER. (c) Electric field and OH^- concentration of Mo-Ni and Ni/Mo-Ni in HER and OER. (d) Schematic illustration of the mechanism of enhanced alkaline water splitting performance.

smooth. As the number of nanoparticles on the smooth substrate increases, more localized electric fields are generated around the nanoparticles. But as the particles get larger, their curvature does not change as much as the small nanoparticles on the smooth-substrated micropillars. This variation of the sample surface roughness (Table S1 and S4) correlates well with the electrocatalytic performance (**Figure S16**), due to the LEF generated around the nanoparticles that impacted the adsorption of OH^- ions onto the electrode surface.

The LEF intensity can be analyzed by OH^- adsorption, as a result of electrostatic interaction (details in the Supporting Information, **Figure S17a**). From **Figure S17b**, Ni/Mo-Ni can be seen to exhibit the lowest OH^- concentration among the sample series at negative electrode potentials, indicating a higher negative electric field than those of Mo-Ni and Ni NPs in HER; whereas at positive electrode potentials the OH^- concentration is the highest on Ni/Mo-Ni, confirming a highest positive electrical field (**Figure S17c**). These results show that the Ni/Mo-Ni has nanoparticles on a smooth substrate due to large changes in curvature, which generate a localized electric field. Therefore, the more ions are adsorbed for reaction to improve the performance. These are in good agreement with the electrocatalytic performance demonstrated above (Figs. 3-5).

4. Conclusion

The Ni/Mo-Ni microrods were prepared by a facile hydrothermal/thermal annealing procedure where Ni nanoparticles were grown onto the Mo-Ni microrod surface. COMSOL simulations showed that the electrical field strength was markedly enhanced around the Ni nanoparticles leading to enhanced H^+ and OH^- adsorption, as compared to the smooth Mo-Ni microrods free of Ni nanoparticles. With this ion-

enhanced environment by LEF, the Ni/Mo-Ni electrode exhibited an ultralow overpotential of −24 mV in HER and + 215 mV in OER at the current density of 10 mA cm^{-2}, and can thus be used as a bifunctional catalyst for water-alkali electrolyzers, which needed only a low cell voltage of 1.50, 1.76, and 1.87 V to drive water splitting at the current density of 10, 100, and 400 mA cm^{-2}, respectively, and stably operate for 87 h. This performance is even better than that based on commercial Pt/C-IrO_2 catalysts. Results from this study may open a new avenue in the design and engineering of Mo-Ni-based electrocatalysts for large-scale hydrogen generation.

Declaration of Competing Interest

The authors declare that they have no known competing financial interests or personal relationships that could have appeared to influence the work reported in this paper.

Acknowledgments

We thank the National Natural Science Foundation of China (Grant No. 21872174, 22002189, 22011530423, and U1932148), International Science and Technology Cooperation Program (Grant No. 2017YFE0127800 and 2018YFE0203402), Hunan Provincial Science and Technology Program (2017XK2026), Hunan Province Key Field R&D Program (2020WK2002), Hunan Provincial Natural Science Foundation of China (2020JJ2041, 2020JJ5691, and 2021JJ308), Shenzhen Science and Technology Innovation Project (Grant No. JCYJ20180307151313532). S.W.C. thanks the US National Science Foundation for partial support of the work (CHE-1900235). We also would like to thank Ting Yang from Shiyanjia Lab (www.shiyanjia.com) for the TEM tests.

Appendix A. Supplementary data

Supplementary data to this article can be found online at https://doi.org/10.1016/j.cej.2022.134860.

References

[1] Z.Y. Yu, Y. Duan, X.Y. Feng, X. Yu, M.R. Gao, S.H. Yu, Clean and affordable hydrogen fuel from alkaline water splitting: past recent progress, and future prospects, Adv. Mater. 33 (2021), e2007100.
[2] H. Li, K. Liu, J. Fu, K. Chen, K. Yang, Y. Lin, B. Yang, Q. Wang, H. Pan, Z. Cai, H. Li, M. Cao, J. Hu, Y.-R. Lu, T.-S. Chan, E. Cortés, A. Fratalocchi, M. Liu, Paired Ru-O-Mo ensemble for efficient and stable alkaline hydrogen evolution reaction, Nano Energy 82 (2021) 1–5767.
[3] Z. Chen, Y. Song, J. Cai, X. Zheng, D. Han, Y. Wu, Y. Zang, S. Niu, Y. Liu, J. Zhu, X. Liu, G. Wang, Tailoring the d-band centers enables Co4 N nanosheets to be highly active for hydrogen evolution catalysis, Angew. Chem. Int. Ed. Engl. 57 (2018) 5076–5080.
[4] H. Shi, Y.T. Zhou, R.Q. Yao, W.B. Wan, X. Ge, W. Zhang, Z. Wen, X.Y. Lang, W. T. Zheng, Q. Jiang, Spontaneously separated intermetallic Co3Mo from nanoporous copper as versatile electrocatalysts for highly efficient water splitting, Nat. Commun. 11 (2020) 2940.
[5] N. Wang, S. Ning, X. Yu, D. Chen, Z. Li, J. Xu, H. Meng, D. Zhao, L. Li, Q. Liu, B. Lu, S. Chen, Graphene composites with Ru-RuO2 heterostructures: Highly efficient Mott–Schottky-type electrocatalysts for pH-universal water splitting and flexible zinc–air batteries, Appl Catals B: Environ 302 (2022), 120838.
[6] S. Chen, C. Lv, L. Liu, M. Li, J. Liu, J. Ma, P. Hao, X. Wang, W. Ding, M. Xie, X. Guo, High-temperature treatment to engineer the single-atom Pt coordination environment towards highly efficient hydrogen evolution, J Energy Chem 59 (2021) 212–219.
[7] P. Chen, X. Hu, High-efficiency anion exchange membrane water electrolysis employing non-noble metal catalysts, Adv. Energy Mater. 10 (39) (2020) 2002285, https://doi.org/10.1002/aenm.v10.3910.1002/aenm.202002285.
[8] X. Wang, Q.i. Hu, G. Li, S. Wei, H. Yang, C. He, Regulation of the adsorption sites of Ni2P by Ru and S co-doping for ultra-efficient alkaline hydrogen evolution, J. Mater. Chem. A 9 (28) (2021) 15648–15653.
[9] Y. Liu, X. Li, Q. Zhang, W. Li, Y.u. Xie, H. Liu, L.u. Shang, Z. Liu, Z. Chen, L. Gu, Z. Tang, T. Zhang, S. Lu, A general route to prepare low-ruthenium-content bimetallic electrocatalysts for pH-universal hydrogen evolution reaction by using carbon quantum dots, Angew. Chem. Int. Ed. Engl. 59 (4) (2020) 1718–1726.
[10] C.-T. Dinh, A. Jain, F.P.G. de Arquer, P. De Luna, J. Li, N. Wang, X. Zheng, J. Cai, B. Z. Gregory, O. Voznyy, B.o. Zhang, M. Liu, D. Sinton, E.J. Crumlin, E.H. Sargent, Multi-site electrocatalysts for hydrogen evolution in neutral media by destabilization of water molecules, Nat. Energy 4 (2) (2019) 107–114.
[11] L. Yu, Q. Zhu, S. Song, B. McElhenny, D. Wang, C. Wu, Z. Qin, J. Bao, Y. Yu, S. Chen, Z. Ren, Non-noble metal-nitride based electrocatalysts for high-performance alkaline seawater electrolysis, Nat. Commun. 10 (2019) 5106.
[12] P. Zhai, Y. Zhang, Y. Wu, J. Gao, B. Zhang, S. Cao, Y. Zhang, Z. Li, L. Sun, J. Hou, Engineering active sites on hierarchical transition bimetal oxides/sulfides heterostructure array enabling robust overall water splitting, Nat. Commun. 11 (2020) 5462.
[13] X. Wang, C. Xu, M. Jaroniec, Y. Zheng, S.Z. Qiao, Anomalous hydrogen evolution behavior in high-pH environment induced by locally generated hydronium ions, Nat. Commun. 10 (2019) 4876.
[14] P. Liu, B.o. Chen, C. Liang, W. Yao, Y. Cui, S. Hu, P. Zou, H. Zhang, H.J. Fan, C. Yang, Tip-Enhanced Electric Field: A New Mechanism Promoting Mass Transfer in Oxygen Evolution Reactions, Adv. Mater. 33 (9) (2021) 2007377, https://doi.org/10.1002/adma.v33.910.1002/adma.202007377.
[15] S. Chen, F. Bi, K. Xiang, Y.u. Zhang, P. Hao, M. Li, B. Zhao, X. Guo, Reactive Template-Derived CoFe/N-Doped Carbon Nanosheets as Highly Efficient Electrocatalysts toward Oxygen Reduction, Oxygen Evolution, and Hydrogen Evolution, ACS Sustain Chem Eng 7 (18) (2019) 15278–15288.
[16] H. Yuan, F. Liu, G. Xue, H. Liu, Y. Wang, Y. Zhao, X. Liu, X. Zhang, L. Zhao, Z. Liu, Laser patterned and bifunctional Ni@N-doped carbon nanotubes as electrocatalyst and photothermal conversion layer for water splitting driven by thermoelectric device, Appl Catal B: Environ 283 (2021), 119647.
[17] J. Yan, Y. Wang, Y. Zhang, S. Xia, J. Yu, B. Ding, Direct magnetic reinforcement of electrocatalytic ORR/OER with electromagnetic induction of magnetic catalysts, Adv. Mater. 33 (2021) 2007525.
[18] Y. Gao, Z. Xiao, D. Kong, R. Iqbal, Q.-H. Yang, L. Zhi, N, P co-doped hollow carbon nanofiber membranes with superior mass transfer property for trifunctional metal-free electrocatalysis, Nano Energy 64 (2019), 103879.
[19] M. Liu, Y. Pang, B. Zhang, P. De Luna, O. Voznyy, J. Xu, X. Zheng, C.T. Dinh, F. Fan, C. Cao, F.P.G. de Arquer, T.S. Safaei, A. Mepham, A. Klinkova, E. Kumacheva, T. Filleter, D. Sinton, S.O. Kelley, E.H. Sargent, Enhanced electrocatalytic CO2 reduction via field-induced reagent concentration, Nature 537 (2016) 382–386.
[20] J. Fu, K. Liu, K. Jiang, H. Li, P. An, W. Li, N. Zhang, H. Li, X. Xu, H. Zhou, D. Tang, X. Wang, X. Qiu, M. Liu, Graphitic Carbon Nitride with Dopant Induced Charge Localization for Enhanced Photoreduction of CO2 to CH4, Adv. Sci. 6 (2019) 1900796.
[21] P. An, L. Wei, H. Li, B. Yang, K. Liu, J. Fu, H. Li, H. Liu, J. Hu, Y.-R. Lu, H. Pan, T.-S. Chan, N. Zhang, M. Liu, Enhancing CO2 reduction by suppressing hydrogen evolution with polytetrafluoroethylene protected copper nanoneedles, J. Mater. Chem. A 8 (31) (2020) 15936–15941.
[22] L. Ma, Y.-L. Chen, X.-P. Song, D.-J. Yang, H.-X. Li, S.-J. Ding, L. Xiong, P.-L. Qin, X.-B. Chen, Structure-Adjustable Gold Nanoingots with Strong Plasmon Coupling and Magnetic Resonance for Improved Photocatalytic Activity and SERS, ACS Appl. Mater. Interfaces 12 (34) (2020) 38554–38562.
[23] A. Nairan, C. Liang, S.-W. Chiang, Y.i. Wu, P. Zou, U. Khan, W. Liu, F. Kang, S. Guo, J. Wu, C. Yang, Proton selective adsorption on Pt–Ni nano-thorn array electrodes for superior hydrogen evolution activity, Energy, Environ Sci 14 (3) (2021) 1594–1601.
[24] Z. Zhuang, J. Huang, Y. Li, L. Zhou, L. Mai, The Holy Grail in Platinum-Free Electrocatalytic Hydrogen Evolution: Molybdenum-Based Catalysts and Recent Advances, ChemElectroChem 6 (14) (2019) 3570–3589.
[25] W. Hua, H.-H. Sun, F. Xu, J.-G. Wang, A review and perspective on molybdenum-based electrocatalysts for hydrogen evolution reaction, Rare Met. 39 (4) (2020) 335–351.
[26] S. Li, E. Li, X. An, X. Hao, Z. Jiang, G. Guan, Transition metal-based catalysts for electrochemical water splitting at high current density: current status and perspectives, Nanoscale 13 (30) (2021) 12788–12817.
[27] Z. Zhang, X. Ma, J. Tang, Porous NiMoO4−x/MoO2 hybrids as highly effective electrocatalysts for the water splitting reaction, J. Mater. Chem. A 6 (26) (2018) 12361–12369.
[28] X. Liu, K. Ni, C. Niu, R. Guo, W. Xi, Z. Wang, J. Meng, J. Li, Y. Zhu, P. Wu, Q.i. Li, J. Luo, X. Wu, L. Mai, Upraising the O 2p Orbital by Integrating Ni with MoO2 for Accelerating Hydrogen Evolution Kinetics, ACS Catal. 9 (3) (2019) 2275–2285.
[29] C. Jian, Q. Cai, W. Hong, J. Li, W. Liu, Edge-Riched MoSe2 /MoO2 Hybrid Electrocatalyst for Efficient Hydrogen Evolution Reaction, Small 14 (13) (2018) 1703798, https://doi.org/10.1002/smll.v14.1310.1002/smll.201703798.
[30] H. Zeng, S. Chen, Y.Q. Jin, J. Li, J. Song, Z. Le, G. Liang, H. Zhang, F. Xie, J. Chen, Y. Jin, X. Chen, H. Meng, Electron Density Modulation of Metallic MoO2 by Ni Doping to Produce Excellent Hydrogen Evolution and Oxidation Activities in Acid, ACS Energy Lett. 5 (6) (2020) 1908–1915.
[31] W. Liang, P. Dong, Z. Le, X. Lin, X. Gong, F. Xie, H. Zhang, J. Chen, N. Wang, Y. Jin, H. Meng, Electron Density Modulation of MoO2/Ni to Produce Superior Hydrogen Evolution and Oxidation Activities, ACS Appl. Mater. Interfaces 13 (2021) 39470–39479.
[32] J. Zhang, T. Wang, P. Liu, Z. Liao, S. Liu, X. Zhuang, M. Chen, E. Zschech, X. Feng, Efficient hydrogen production on MoNi4 electrocatalysts with fast water dissociation kinetics, Nat. Commun. 8 (2017) 15437.
[33] J. Cao, H. Li, R. Zhu, L. Ma, K. Zhou, Q. Wei, F. Luo, Improved hydrogen generation via a urea-assisted method over 3D hierarchical NiMo-based composite microrod arrays, J. Alloy. Compd. 844 (2020), 155382.
[34] Y. Chen, J. Yu, J. Jia, F. Liu, Y. Zhang, G. Xiong, R. Zhang, R. Yang, D. Sun, H. Liu, W. Zhou, Metallic Ni3Mo3N Porous Microrods with Abundant Catalytic Sites as Efficient Electrocatalyst for Large Current Density and Superstability of Hydrogen

Evolution Reaction and Water Splitting, Appl. Catal. B 272 (2020) 118956, https://doi.org/10.1016/j.apcatb.2020.118956.
[35] B. Zhang, L. Zhang, Q. Tan, J. Wang, J. Liu, H. Wan, L. Miao, J. Jiang, Simultaneous interfacial chemistry engineering and inner Helmholtz plane regulating for superior alkaline hydrogen evolution, Energy, Environ Sci 13 (2020) 3007–3013.
[36] Z.-Y. Yu, C.-C. Lang, M.-R. Gao, Y. Chen, Q.-Q. Fu, Y. Duan, S.-H. Yu, Ni–Mo–O nanorod-derived composite catalysts for efficient alkaline water-to-hydrogen conversion via urea electrolysis, Energy, Environ Sci 11 (2018) 1890–1897.
[37] F. Yang, Y. Luo, Q. Yu, Z. Zhang, S. Zhang, Z. Liu, W. Ren, H.M. Cheng, J. Li, B. Liu, A Durable and Efficient Electrocatalyst for Saline Water Splitting with Current Density Exceeding 2000 mA cm^{-2}, Adv. Funct. Mater. 31 (2021) 2010367.
[38] J.A. Rodriguez, S. Chaturvedi, J.C. Hanson, A. Albornoz, J.L. Brito, Electronic Properties and Phase Transformations in $CoMoO_4$ and $NiMoO_4$: XANES and Time-Resolved Synchrotron XRD Studies, J. Phys. Chem. B 102 (1998) 1347–1355.
[39] A. Nairan, P. Zou, C. Liang, J. Liu, D. Wu, P. Liu, C. Yang, NiMo Solid Solution Nanowire Array Electrodes for Highly Efficient Hydrogen Evolution Reaction, Adv. Funct. Mater. 29 (2019) 1903747.
[40] S. Sajjad, C. Wang, X. Wang, T. Ali, T. Qian, C. Yan, In situ evolved NiMo/NiMoO4 nanorods as a bifunctional catalyst for overall water splitting, Nanotechnology 31 (2020), 495404.
[41] Y.-Y. Chen, Y. Zhang, X. Zhang, T. Tang, H. Luo, S. Niu, Z.-H. Dai, L.-J. Wan, J.-S. Hu, Self-Templated Fabrication of MoNi4 /MoO3-x Nanorod Arrays with Dual Active Components for Highly Efficient Hydrogen Evolution, Adv. Mater. 29 (39) (2017) 1703311, https://doi.org/10.1002/adma.201703311.
[42] H.J.W. Li, H. Zhou, K. Chen, K. Liu, S. Li, K. Jiang, W. Zhang, Y. Xie, Z. Cao, H. Li, H. Liu, X. Xu, H. Pan, J. Hu, D. Tang, X. Qiu, J. Fu, M. Liu, Metallic MoO2-Modified Graphitic Carbon Nitride Boosting Photocatalytic CO2 Reduction via Schottky Junction, Solar RRL 4 (8) (2020) 1900416, https://doi.org/10.1002/solr.v4.810.1002/solr.201900416.
[43] X.i. Wang, C. Liu, C. Gao, K. Yao, S.S.M. Masouleh, R. Berté, H. Ren, L.d. S. Menezes, E. Cortés, I.C. Bicket, H. Wang, N. Li, Z. Zhang, M. Li, W. Xie, Y. Yu, Y. Fang, S. Zhang, H. Xu, A. Vomiero, Y. Liu, G.A. Botton, S.A. Maier, H. Liang, Self-Constructed Multiple Plasmonic Hotspots on an Individual Fractal to Amplify Broadband Hot Electron Generation, ACS Nano 15 (6) (2021) 10553–10564.
[44] Z. Xu, S. Jin, M.H. Seo, X. Wang, Hierarchical Ni-Mo2C/N-doped Carbon Mott-Schottky Array for Water Electrolysis, Appl Catal B: Environ 292 (2021) 120168, https://doi.org/10.1016/j.apcatb.2021.120168.
[45] J. Park, H. Kim, G.H. Han, J. Kim, S.J. Yoo, H.-J. Kim, S.H. Ahn, Electrochemically fabricated MoO3–MoO2@NiMo heterostructure catalyst with Pt-like activity for the pH-universal hydrogen evolution reaction, J. Mater. Chem. A 9 (6) (2021) 3677–3684.
[46] G. Chen, HuangJingWei Li, Y. Zhou, C. Cai, K. Liu, J. Hu, H. Li, J. Fu, M. Liu, CoS2 needle arrays induced a local pseudo-acidic environment for alkaline hydrogen evolution, Nanoscale 13 (32) (2021) 13604–13609.
[47] D. Liu, X. Li, S. Chen, H. Yan, C. Wang, C. Wu, Y.A. Haleem, S. Duan, J. Lu, B. Ge, P. M. Ajayan, Y.i. Luo, J. Jiang, L.i. Song, Atomically dispersed platinum supported on curved carbon supports for efficient electrocatalytic hydrogen evolution, Nat. Energy 4 (6) (2019) 512–518.